IPP-Report

Max-Planck-Institut
für Plasmaphysik

E. Strumberger, H. Wobig, J. Kißlinger, C. Nührenberg

Equilibrium and Stability Properties of a Helias Reactor

IPP III/249
September 1999

Max-Planck-Institut für Plasmaphysik

Equilibrium and Stability Properties of a Helias Reactor

E. Strumberger, H. Wobig, J. Kißlinger, C. Nührenberg[1]

Max–Planck–Institut für Plasmaphysik, *IPP-EURATOM* Association
D–85748 Garching bei München, Germany

[1] Max–Planck–Institut für Plasmaphysik, Teilinstitut Greifswald
D–17489 Greifswald, Germany

IPP III/249 September 1999

Table of contents

Abstract

A low-shear Helias (Helical Advanced Stellarator) configuration is studied with respect to its usefulness for a Helias reactor. Its equilibrium properties and its MHD stability properties, that is Mercier and resistive interchange criteria, local ballooning modes and global ideal MHD stability, are investigated using an extensive numerical code system. From the results a set of design values of the reactor plasma is derived.

1.0 Introduction

Helias (Helical Advanced Stellarator) configurations are studied at the IPP Garching with respect to their potential as a fusion reactor. In this report we investigate the equilibrium and stability properties of a Helias configuration up to a volume-averaged β-value of $\langle\beta\rangle = 5\%$. For $\langle\beta\rangle$= 1, 2, 3, 4 and 5% free-boundary equilibria are computed, and Mercier and resistive interchange criteria, local ballooning modes and global ideal MHD stability are studied using an extensive numerical code system.

The Helias reactor is characterized by a major radius of $R_0 = 22$ m, a plasma radius of $a_0 = 1.8$ m and the vacuum magnetic field amounts to 4.75 T on the magnetic axis. In the plasma centre the rotational transform decreases with increasing plasma β, so that low rational values of the rotational transform may appear for higher β-values. In order to avoid the 5/6 resonance, a vacuum magnetic field with low shear has been designed. Its rotational transform value on the magnetic axis amounts to $\iota = 0.875$ and it rises to $\iota = 5/5$ in the edge region. There, five macroscopic islands surround the last closed magnetic surface (LCMS). The mirror field of the vacuum field amounts to approximately 10%, which is needed to improve the α particle confinement.

This report is organized as follows. In Section 2 the code system is described which has been used for these numerical computations. The vacuum magnetic field is the subject of Section 3. There, the coil system is described in Section 3.1 and the properties of the vacuum field are discussed in Section 3.2. Section 4 deals with the iterative computation of the finite-β equilibria and the properties of the corresponding magnetic fields. The MHD stability properties of these equilibria are investigated in Section 5, where the Mercier and resistive interchange criteria (Section 5.1), the local ballooning modes (Section 5.2) and the global ideal MHD stability properties (Section 5.3) are studied. Finally, in Section 6 the results are summarized and a set of design values of the reactor plasma is derived.

2.0 The code system

For the following computations a code system is necessary which makes use of work stations, a T3E parallel computer and a SX5 vector computer. Figure 1 gives an overview over this code system.

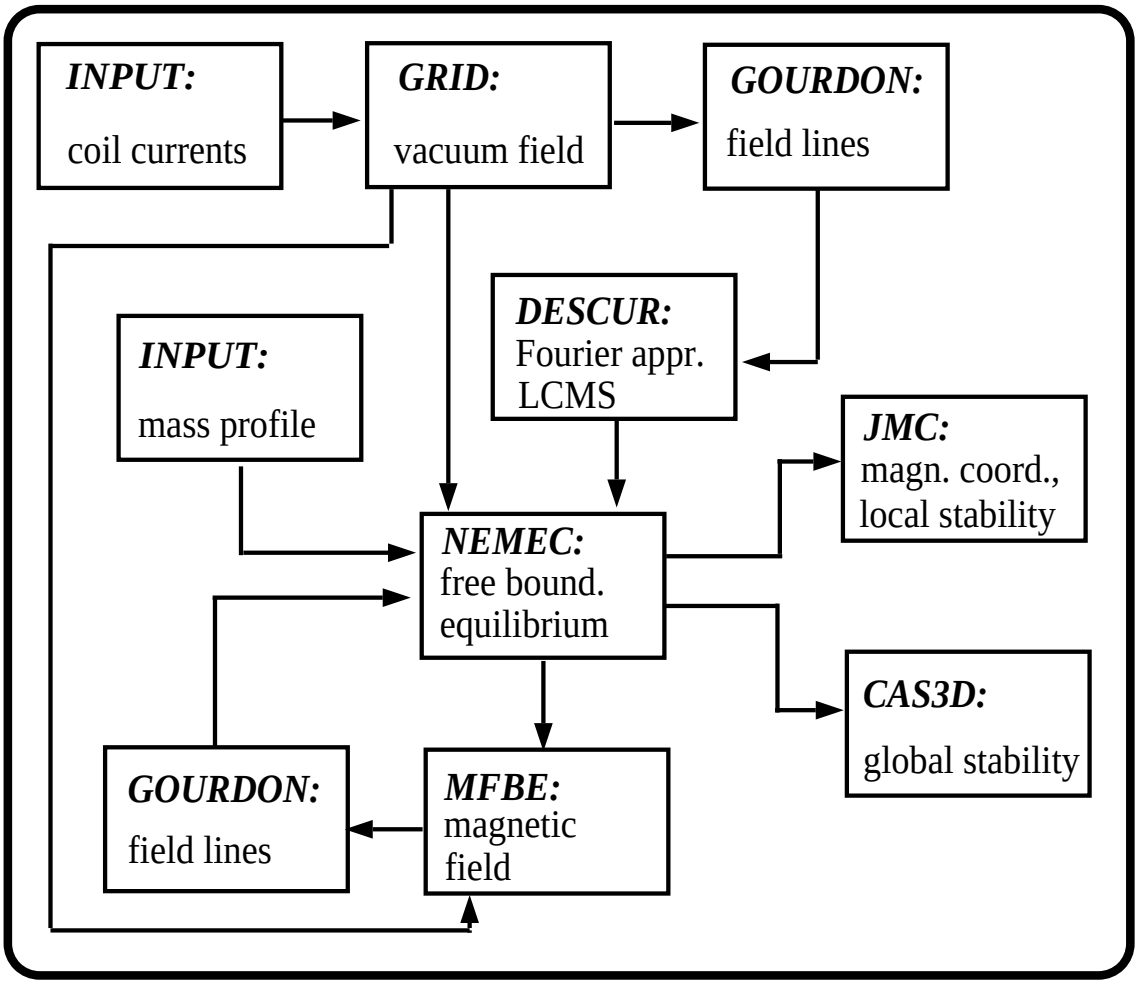

FIG. 1: Overview of the code system

Starting from given coil currents the vacuum magnetic field is computed on a grid with a fully parallelized code named GRID. This vacuum magnetic field serves as input to the GOURDON, NEMEC and MFBE codes.

The GOURDON code is used for field line tracing. In addition to Poincaré plots of the magnetic field, the GOURDON code yields the rotational transform and the magnetic well of the magnetic field. Furthermore, the LCMS is determined.

The data of the coordinates along the field line forming the LCMS are used in the DESCUR code [1]. This code computes the Fourier representation of the LCMS which serves as input to the NEMEC code.

The 3D free-boundary equilibrium NEMEC code [2,3] (NEMEC = VMEC + NESTOR [4]) computes three-dimensional free-boundary finite-β Helias equilibria. For a given mass profile it yields the Fourier coefficients of the nested flux surfaces inside and on the plasma boundary, the Fourier coefficients of the magnetic field on these flux surfaces and the Fourier coefficients of the potential Φ on the plasma boundary which determines the magnetic field outside the plasma boundary. For these computations a SX5 computer is used.

The MFBE code [5] calculates the magnetic field of the plasma equilibrium inside and outside the plasma boundary on a grid. This magnetic field serves as input to the GOURDON code, which is used to determine the LCMS of the field. If this LCMS does not coincide with the plasma boundary obtained by the NEMEC code, the toroidal flux, which is a free parameter in the NEMEC code, is modified, i.e. the toroidal flux is determined iteratively. The fully parallelized MFBE code works very fast on a T3E computer.

Investigations of Mercier and resistive interchange criteria and local ballooning modes are made with the JMC code [6]. This code has also been parallelized and is now used on a T3E computer.

The global ideal MHD stability is studied by using the CAS3D code [7]. This is a 3D stability code for a nonlocal mode analysis based on the formulation of the MHD energy functional in magnetic coordinates [8].

3.0 The vacuum magnetic field

3.1 The coil system

The coil system consists of five field periods with ten modular coils per period producing a vacuum magnetic field of 4.75 T on the magnetic axis. In comparison to a previous design [9] the geometry of the coils has been slightly changed in order to reduce the shear and to increase the magnetic mirror. Parameters of the HSR_B coil system are summed up in Table I, and Fig. 2 shows the winding packs of the coils for one period.

TABLE I: Properties of the HSR_B coil system

Major radius	22	m
Number of coils	50	
Average coil radius	5	m
Maximum field on coils	10	T
Current density	29.5	MA/m^2
Windings per coil	288	
Current in winding	37.5	kA
Magnetic energy	100	GJ
Mass of one coil	200	tons
SC winding pack	41	tons

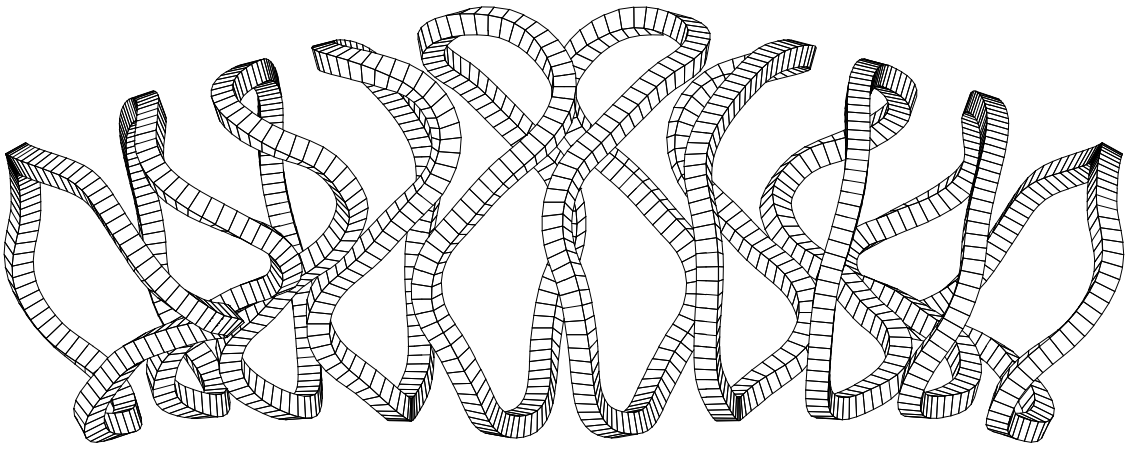

FIG. 2: HSR_B coil system for one period. The cross-section of a winding pack amounts to 0.6 x 0.62 m.

3.2 Properties of the vacuum magnetic field

The vacuum magnetic field structure is plotted in Fig. 3. There, the Poincaré plots at the bean-shaped cross-section ($\varphi = 0^o$) and the triangular cross-section ($\varphi = 36^o$) are shown. The red dots mark the LCMS and the five macroscopic islands are given in green. There exist further closed surfaces (black dots) outside these islands, but in a future reactor device divertor plates will intersect the macroscopic islands, so that the last closed magnetic surface inside these islands will act as plasma boundary. Finally, the blue dots characterize the ergodized region.

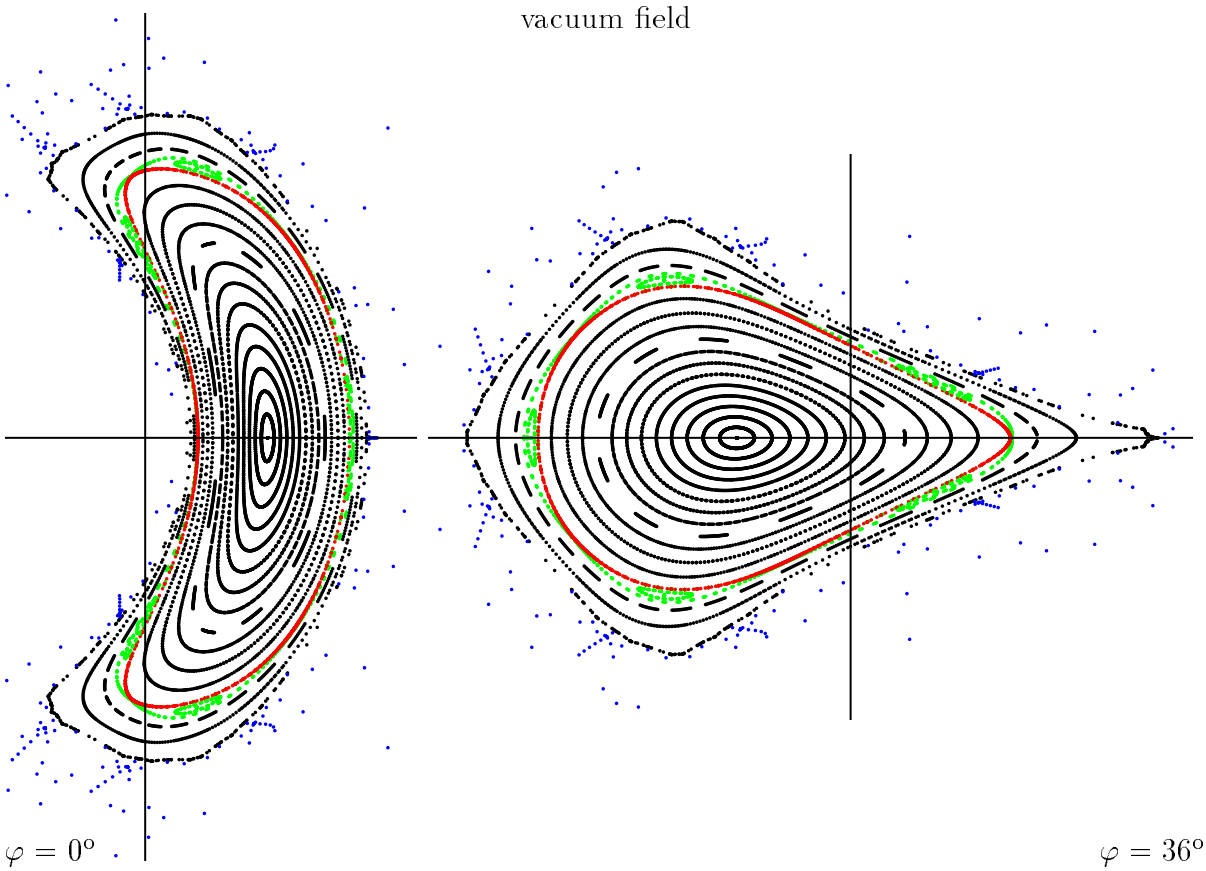

FIG. 3: Poincaré plots of the vacuum magnetic field. At the symmetric bean-shaped and triangular cross-sections flux surfaces (black dots), a chain of five islands (green dots), the last closed magnetic surface (red dots) and ergodic field lines (blue dots) are plotted.

The rotational transform profile and the magnetic well are plotted in Figs 4 and 5. Because of the low shear the rotational transform profile is flat in the plasma centre. It increases from $\iota = 0.875$ on the magnetic axis to $\iota = 5/5$ in the edge region. The

magnetic well $V'' = (V'_{LCMS} - V'_0)/V'_0$ (V'_{LCMS} = specific volume on the LCMS, V'_0 = specific volume on the magnetic axis) amounts to 0.68%.

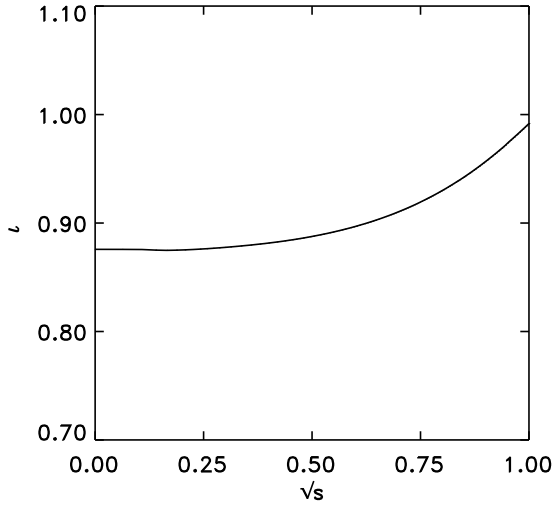

FIG. 4: Rotational transform profile of the vacuum magnetic field.

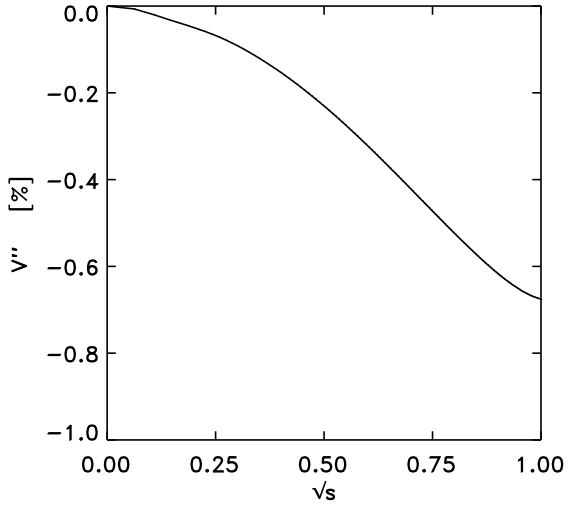

FIG. 5: Magnetic well of the vacuum magnetic field.

The Fourier representation of the magnetic field B in magnetic coordinates [8] is given by

$$B = \sum_{\mathrm{m,n}} B_{\mathrm{m,n}}(s)\cos[2\pi(\mathrm{m}\theta - \mathrm{n}\phi)],$$

with s being the normalized flux label and θ, ϕ being the poloidal and toroidal variables. Figure 6 shows the Fourier coefficients $B_{\mathrm{m,n}}$ versus $\sqrt{s}$. There, $B_{0,0}$ describes the main magnetic field containing the deepening of the magnetic well, $B_{1,0}$ represents the mirror field ($\approx 10\%$), $B_{0,1}$ the toroidal curvature and $B_{1,1}$ the helical curvature.

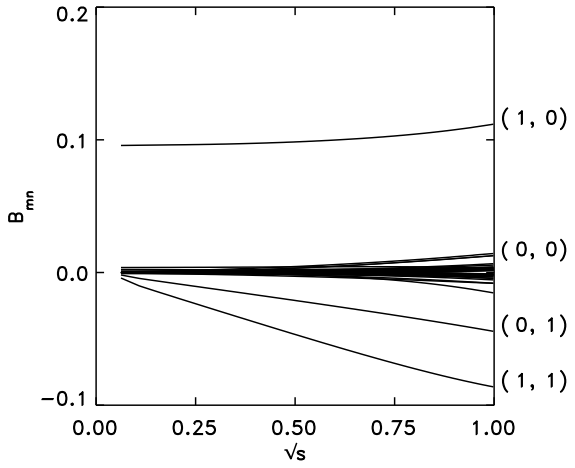

FIG. 6: The $B_{\mathrm{m,n}}$'s are plotted versus $\sqrt{s}$. $B_{0,0}(s = 0) = 1$ has been subtracted in plotting $B_{0,0}$.

4.0 Finite-β equilibria

Three-dimensional free-boundary equilibria and the corresponding magnetic fields are computed self-consistently for various β-values up to $\langle\beta\rangle = 5\%$ by means of the NEMEC, MFBE and GOURDON codes [5]. In order to compute free-boundary equilibria a mass profile $m(s)$ has to be provided as input to the NEMEC code. For the following computations a mass profile of the form

$$m(s) = a_0(1 - \frac{11}{7}s + \frac{4}{7}s^2),$$

has been chosen. The constant a_0 depends on the desired β-value. The adiabatic conservation of the mass between neighbouring flux surfaces requires for the pressure profile $p(s)$ [10]

$$p(s) = m(s)(V'(s))^{-\gamma},$$

with $V'(s)$ being the differential volume element and γ ($\gamma = 2$) being the adiabatic index. With increasing β the pressure profile differs only slightly from the mass profile which has been assumed to be the same for all considered β-values. Figure 7 shows the mass profile and the pressure profile for $\langle\beta\rangle = 5\%$.

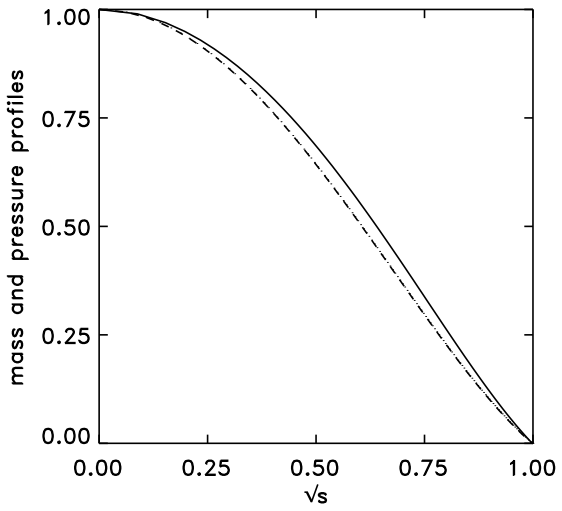

FIG. 7: Mass profile (dashed curve) and pressure profile (solid curve) for $\langle\beta\rangle = 5\%$.

FIG. 8: Poincaré plots of the magnetic fields for $\langle\beta\rangle = 2, 3, 4$ and 5% (see pages 9 and 10). At the symmetric bean-shaped ($\varphi = 0^o$) and triangular ($\varphi = 36^o$) cross-sections flux surfaces (black dots), macroscopic islands (green dots), the last closed magnetic surface (red dots) and stochastic field lines (blue dots) are plotted.

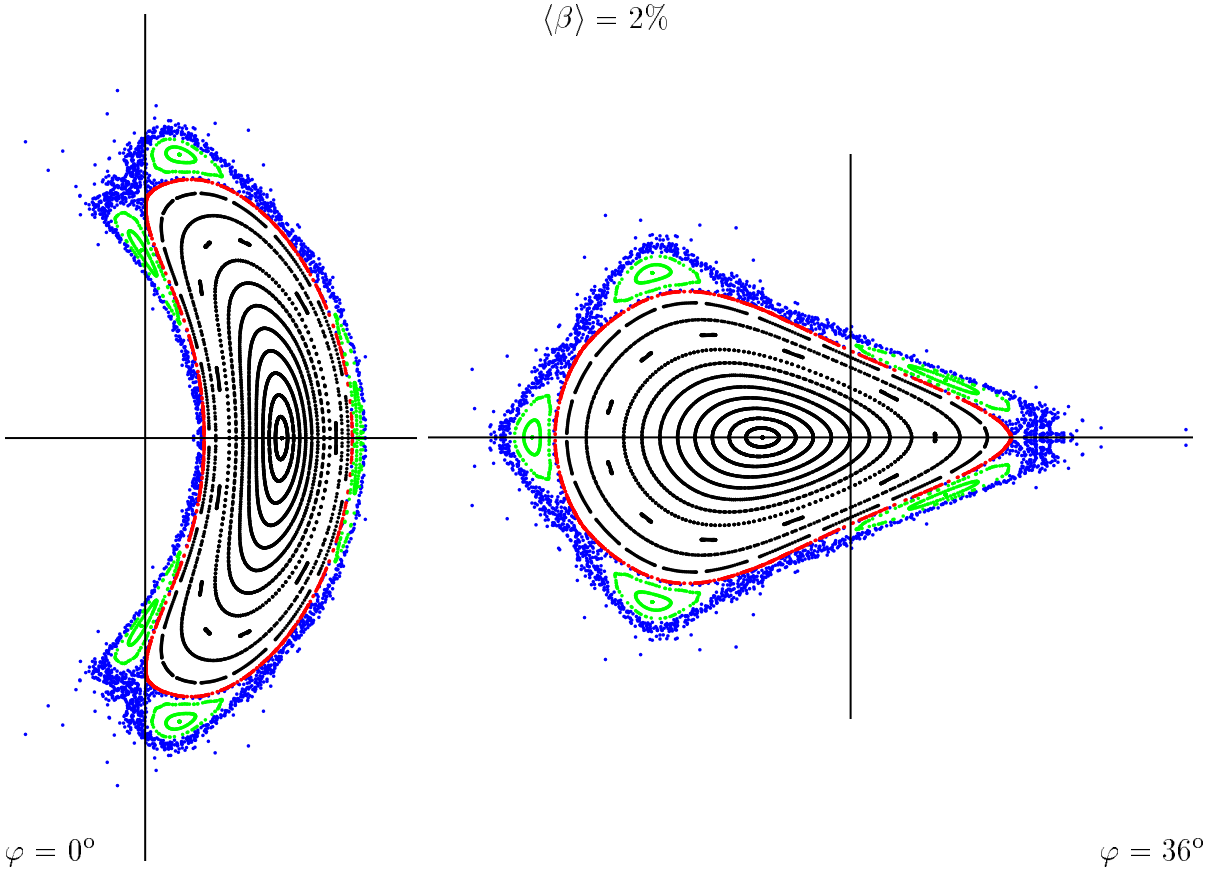
$\langle\beta\rangle = 2\%$
$\varphi = 0^{\rm o}$
$\varphi = 36^{\rm o}$

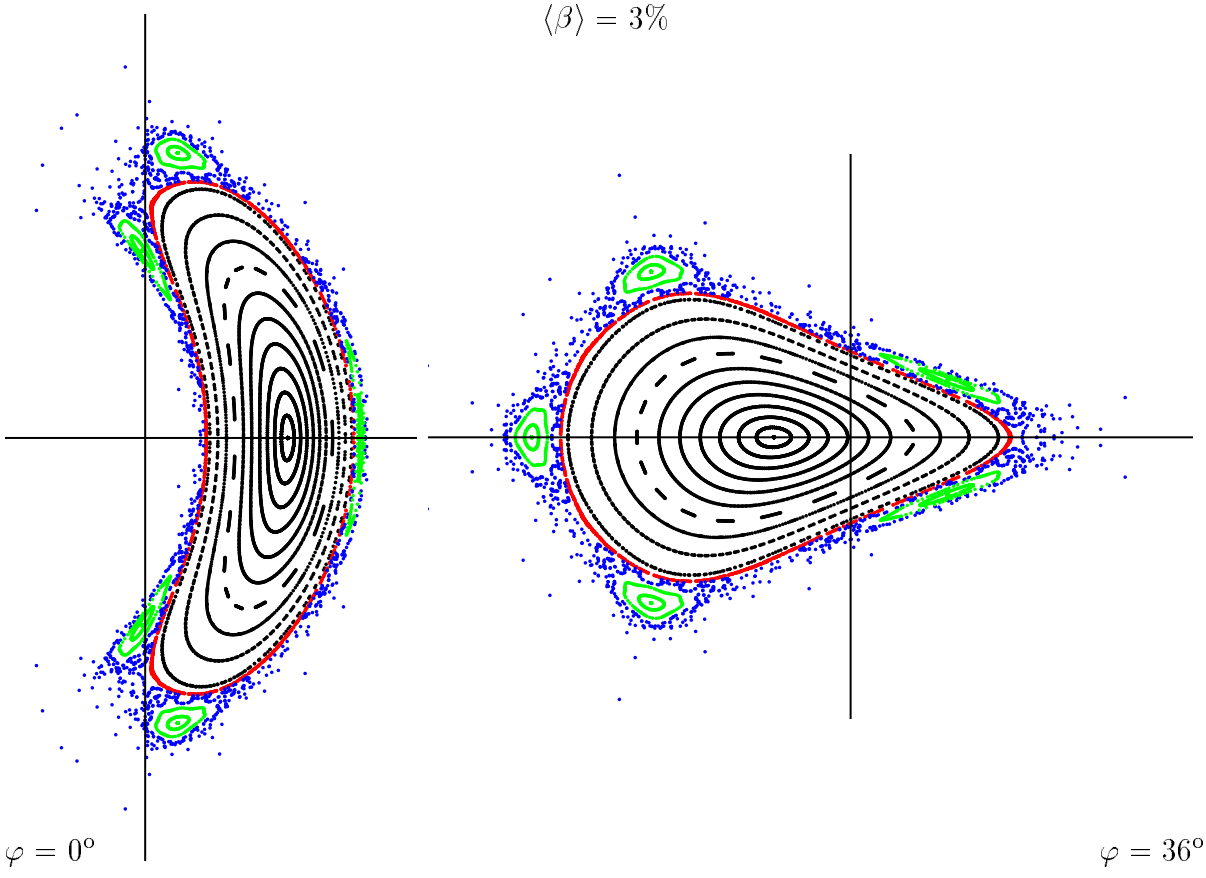
$\langle\beta\rangle = 3\%$
$\varphi = 0^{\rm o}$
$\varphi = 36^{\rm o}$

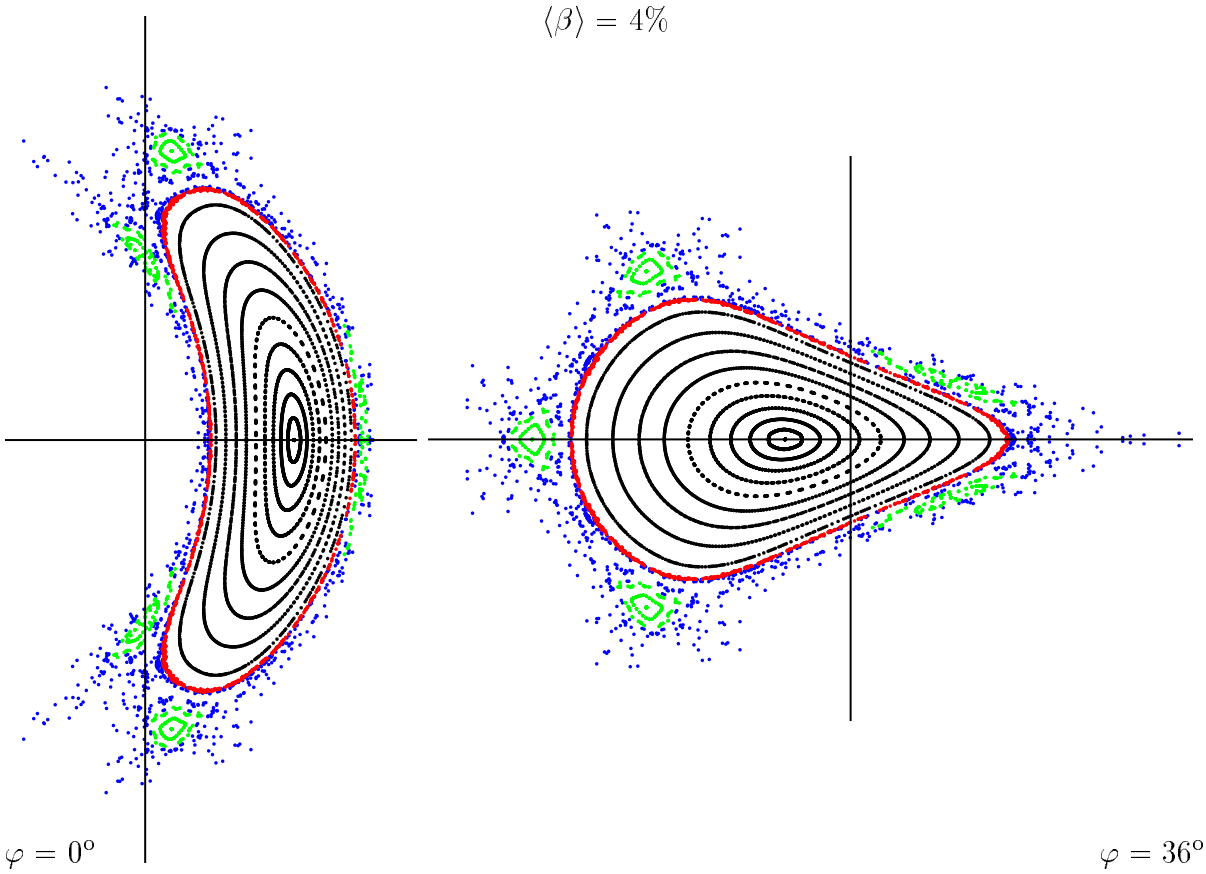
$\langle\beta\rangle = 4\%$
$\varphi = 0^{\circ}$
$\varphi = 36^{\circ}$

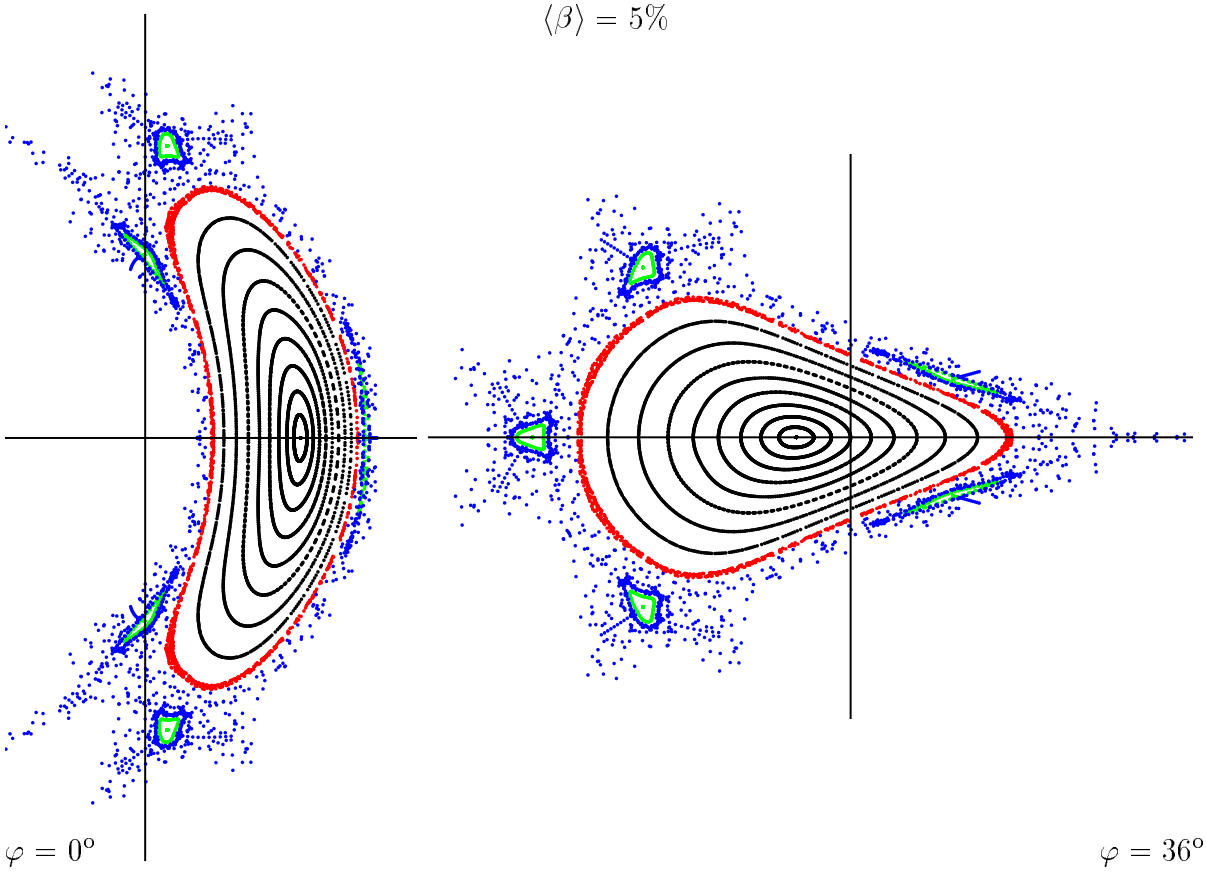
$\langle\beta\rangle = 5\%$
$\varphi = 0^{\circ}$
$\varphi = 36^{\circ}$

Figure 8 shows the magnetic fields for $\langle\beta\rangle = 2, 3, 4$ and 5%. The edge region ergodizes for $\langle\beta\rangle \geq 2\%$. The width of the 5/5 islands increases with β, while the positions of the X- and O-points of these macroscopic islands stay almost unchanged. This is a favourable behaviour with respect to divertor operation.

Comparisons of the resulting finite-β magnetic fields with the corresponding vacuum field yield informations about the variations of the Shafranov shift, the aspect ratio, the magnetic well and the ι-profile with increasing plasma β. Table II contains the values of the rotational transform on the magnetic axis, the Shafranov shift, the plasma volume, the aspect ratio and the magnetic well in dependence on $\langle\beta\rangle$.

TABLE II: Rotational transform ι_0 on the magnetic axis, Shafranov shift $\Delta R/a_0$ (ΔR = mean shift of the magnetic axis, a_0 = plasma radius), volume V enclosed by the LCMS, aspect ratio A and magnetic well V'' for various $\langle\beta\rangle$.

$\langle\beta\rangle$ [%]	ι_0	$\Delta R/a_0$ [%]	V [m^3]	A	V'' [%]
0	0.875	-	1828.4	10.60	0.68
1	0.867	6.3	1744.3	10.98	2.59
2	0.860	12.3	1681.6	11.20	4.37
3	0.849	18.1	1623.5	11.45	6.00
4	0.837	23.4	1570.5	11.68	7.61
5	0.820	28.9	1521.3	11.91	9.14

One of the main results is the small Shafranov shift. It is in the expected range of a Helias configuration and fulfills the requirement of a fusion reactor. From this point of view a further optimization of Helias configurations is not necessary. Further, equilibria with a sufficient plasma volume exist up to $\langle\beta\rangle = 5\%$.

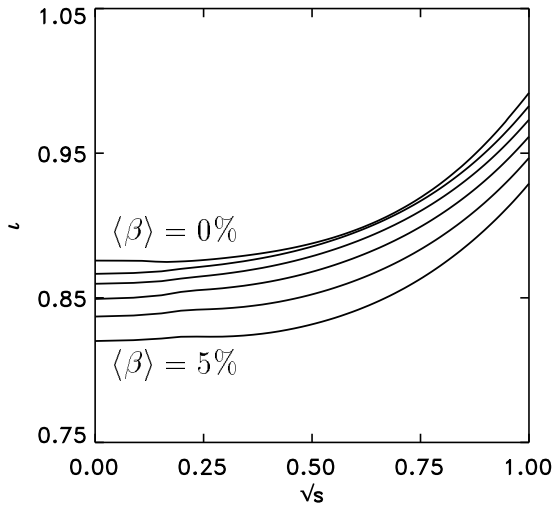

FIG. 9: Rotational transform profiles ι for $\langle\beta\rangle$ = 0 (upper curve), 1, 2, 3, 4 and 5% (lower curve) versus $\sqrt{s}$ with s being the normalized flux label. The rotational transform decreases with increasing β.

Figure 9 illustrates the behaviour of the ι-profile. The rotational transform decreases with rising plasma pressure leading to the existence of low rational values ($\iota = 5/6$) in the plasma centre for $\langle\beta\rangle \geq 4.2\%$.

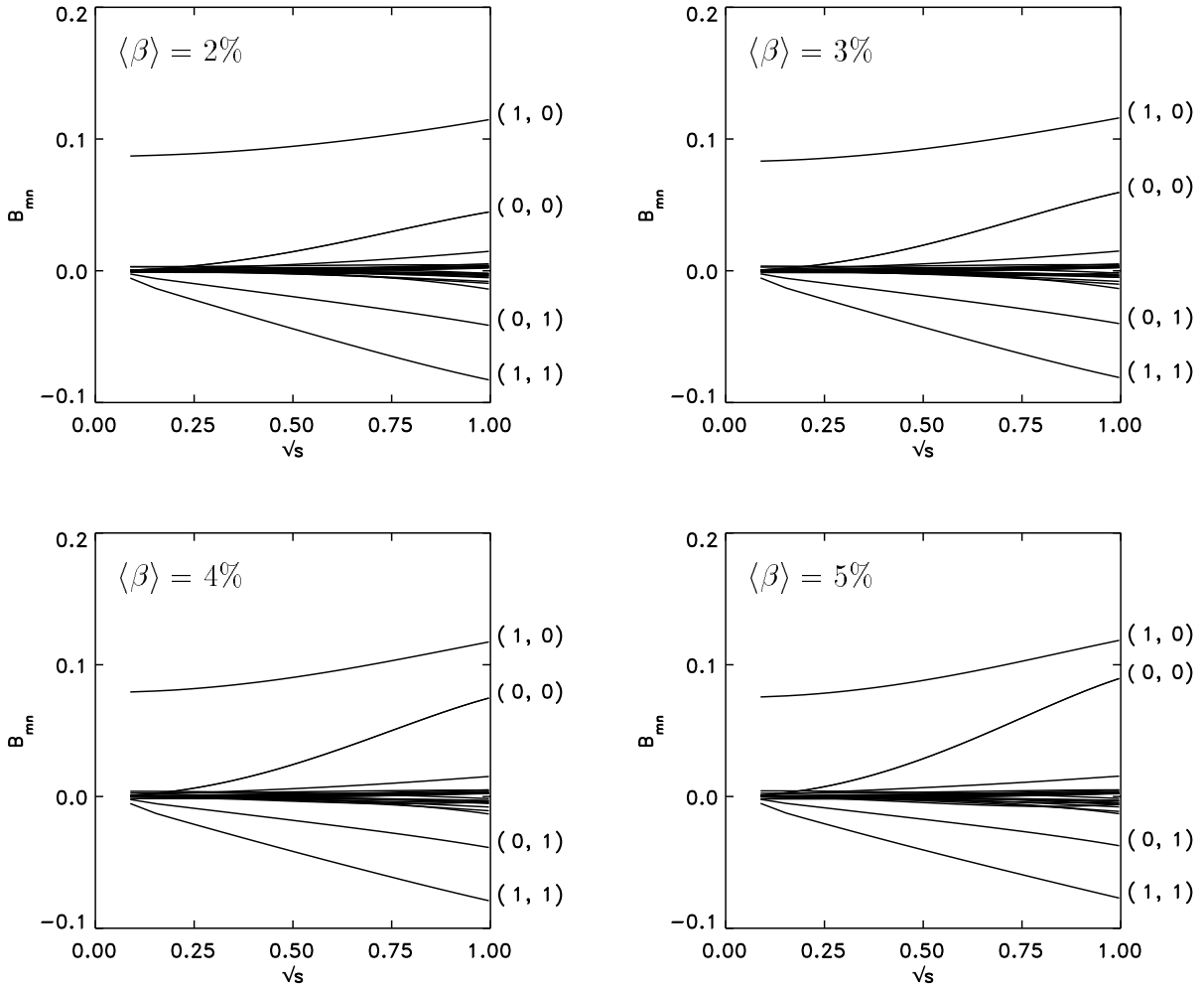

FIG. 10: The $B_{\mathrm{m,n}}$'s are plotted versus $\sqrt{s}$ for $\langle\beta\rangle = 2, 3, 4$ and 5%. $B_{0,0}(s = 0) = 1$ has been subtracted in plotting $B_{0,0}$.

Figure 10 shows the $B_{\mathrm{m,n}}$'s as functions of $\sqrt{s}$ for $\langle\beta\rangle = 2, 3, 4$ and 5%. There, the component $B_{0,0}$ shows the largest dependency on the plasma beta because of the deepening of the magnetic well with increasing β. The variation with β decreases with increasing mode number. The weak β-dependency is a consequence of the small change in geometry of the flux-surfaces as β is increased (see Fig. 8), which itself is due to the small Pfirsch-Schlüter current density of this optimized HSR configuration.

5.0 MHD stability properties

5.1 Mercier and resistive interchange criteria

Local MHD stability properties of the finite-β equilibria are studied with respect to the Mercier [11] and resistive interchange [12] criteria by means of the JMC code [6, 13].

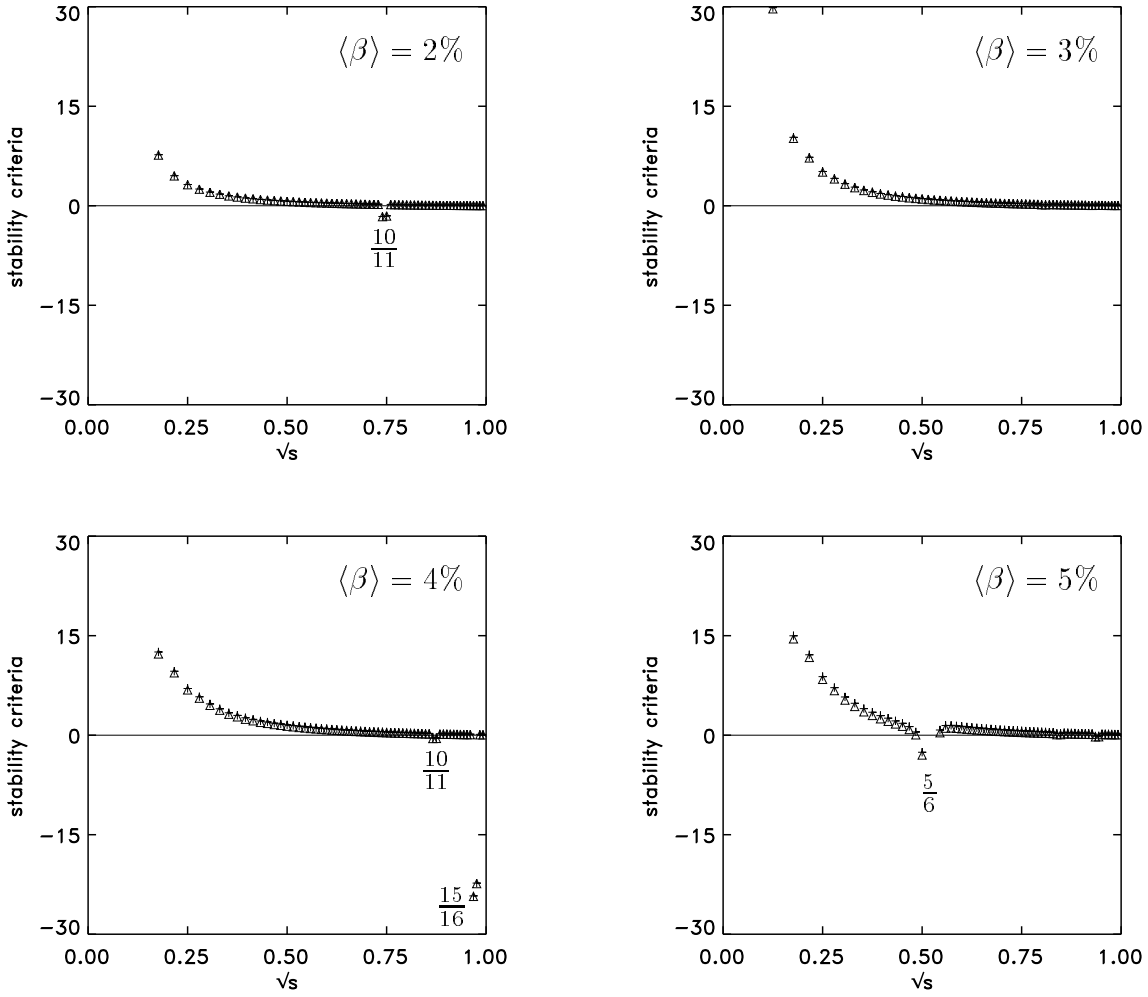

FIG. 11: Mercier (+) and resistive interchange (Δ) versus $\sqrt{s}$ for $\langle\beta\rangle = 2, 3, 4$ and 5%.

Figure 11 shows the Mercier and resistive interchange criteria for $\langle\beta\rangle = 2, 3, 4$ and 5%. Since the magnetic coordinates have been computed for m=0,1,...,23 poloidal and n=-24,...,0,...,24 toroidal Fourier coefficients, higher resonances like m/n=15/16 could be resolved. While the high resonances (m/n=10/11, m/n=15/16) are located around a single flux surface, a finite region of instability prevails around $\sqrt{s} = 0.5$ for $\langle\beta\rangle = 5\%$. There, the low resonance m/n=5/6 occurs.

5.2 Local ballooning modes

For various mode numbers the ballooning modes have been computed for $\langle\beta\rangle = 1, 2, 3, 4$ and 5%. The ballooning stability behaviour is characterized by the solution of the one-dimensional ballooning equation [13, 6] on field lines with rational rotational transform value. If the solution passes through zero the equilibrium is locally ballooning unstable. Here, the ballooning equation has been solved up to the point where the field line becomes closed in toroidal direction. The asymptotic behaviour of the solution has not been investigated.

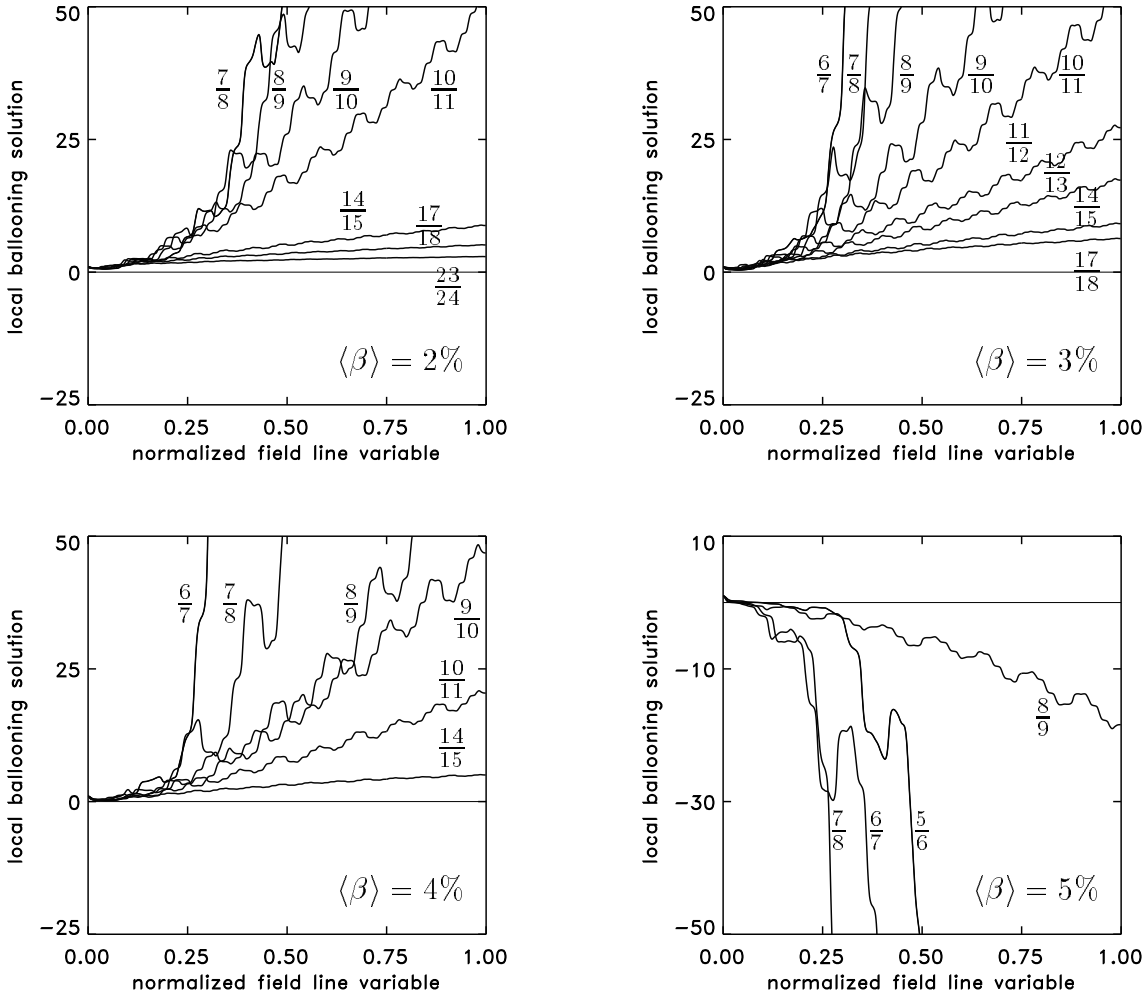

FIG. 12: Local ballooning solutions along rational, i.e. toroidally closed, normalized field lines for $\langle\beta\rangle = 2, 3, 4$ and 5%. The numbers give the rotational transform values of the field lines.

In Fig. 12 the solution of the local ballooning equation is plotted for various mode numbers and $\langle\beta\rangle = 2, 3, 4$ and 5%. For $\langle\beta\rangle \leq 4\%$ the equilibria are stable with respect to local ballooning modes, while for $\langle\beta\rangle = 5\%$ the equilibrium is unstable.

5.3 Global ideal MHD stability properties

The equilibrium with $\langle\beta\rangle = 4\%$ has been investigated with respect to the global MHD stability by using the CAS3D code [7] in its fixed-boundary version CAS3D2 which uses the incompressibility constraint on the MHD displacement vector. In order to assess the stability of a single equilibrium here a 1-parametric sequence of stability calculations has been generated by artificially varying the amount of the main stabilizing term, such that for vanishing sequence parameter the stabilizing terms are considerably reduced and that for sequence parameter unity the full MHD energy functional is obtained. Various perturbation Fourier tables have been used, especially including both mode families present in a 5-periodic device. The computation parameters have been chosen to be comparable to those used for the investigation of the W7-X stability [14] (64 radial grid points, 115 perturbation Fourier harmonics, N=2 mode family).

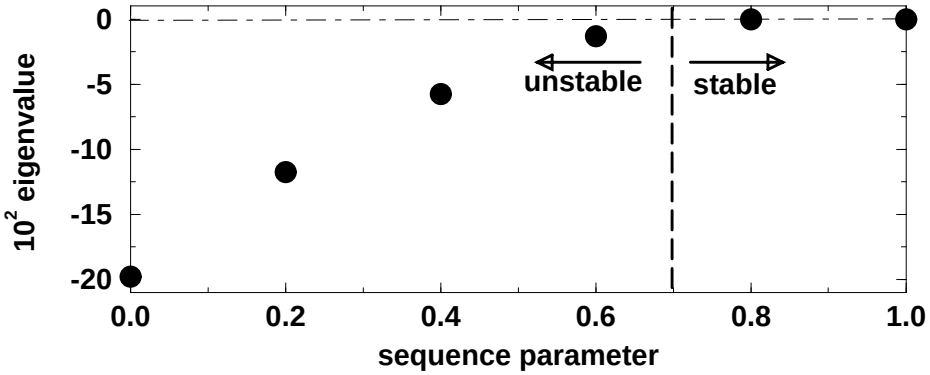

FIG. 13: Result of a global ideal MHD stability study of the $\langle\beta\rangle = 4\%$ equilibrium: CAS3D2 eigenvalues versus an artificially introduced factor which was applied to the main stabilizing term in the MHD energy functional, so that for sequence parameter unity the full MHD energy functional is obtained. The stability limit is reached at approximately 0.7 in the sequence parameter.

As an example Fig. 13 shows CAS3D2 eigenvalues as obtained in such series of calculations for N=2 mode family perturbations. The results show that in this sequence a stability limit is obtained for a value of the sequence parameter of approximately 0.7. Similar results have been obtained for the N=1 mode family, so that it may be concluded that this equilibrium is stable with a good safety margin.

For a sequence parameter smaller than 0.7 instability prevails. By way of example Fig. 14 shows the perturbed pressure distribution for sequence parameter 0.6 at the bean-shaped cross-section. This case is dominated by the m=9, n=-8 harmonic. Note

that for the incompressible perturbations which are used here the perturbed pressure is proportional to the scalar normal component of the displacement vector.

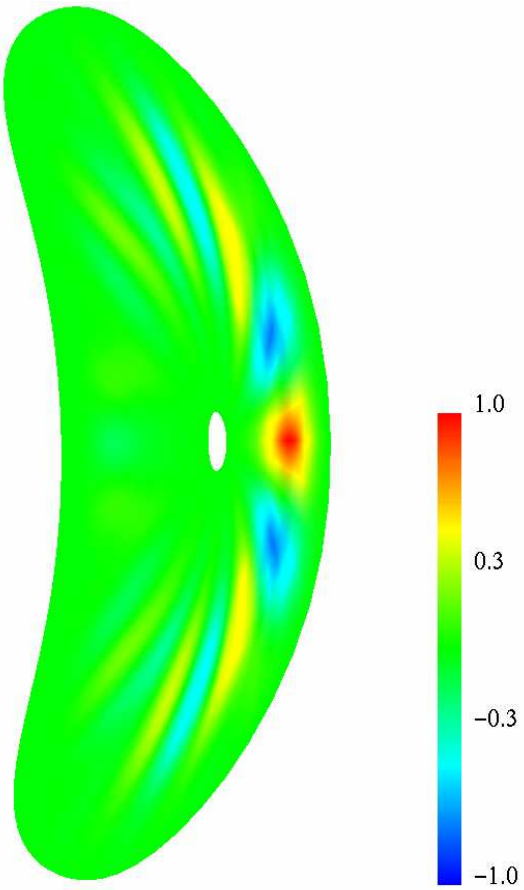

Fig. 14: Perturbed pressure for the essentially m=9, n=-8 perturbation for the stable $\langle\beta\rangle = 4\%$ HSR equilibrium. Note, that this perturbation is unstable only because of an artificially lowered stabilizing contribution to the MHD energy functional. Computation parameters: 64 radial grid points, 115 perturbation Fourier harmonics, N=2 mode family, sequence parameter 0.6.

6.0 Summary

The results of the computations can be summed up in the following statements:

- Equilibria with sufficient plasma volume exist up to $\langle\beta\rangle = 5\%$.
- The edge region ergodizes for $\langle\beta\rangle \geq 2\%$.
- The width of the 5/5 islands increases with β, while the positions of their X- and O-points are almost unchanged $\rightarrow$ favourable behaviour with respect to divertor operation.
- The Shafranov shift is sufficiently small under reactor conditions.
- The rotational transform decreases with rising plasma pressure $\rightarrow \iota = 5/6$ appears around $\langle\beta\rangle = 4.2\%$ (see Fig. 15).

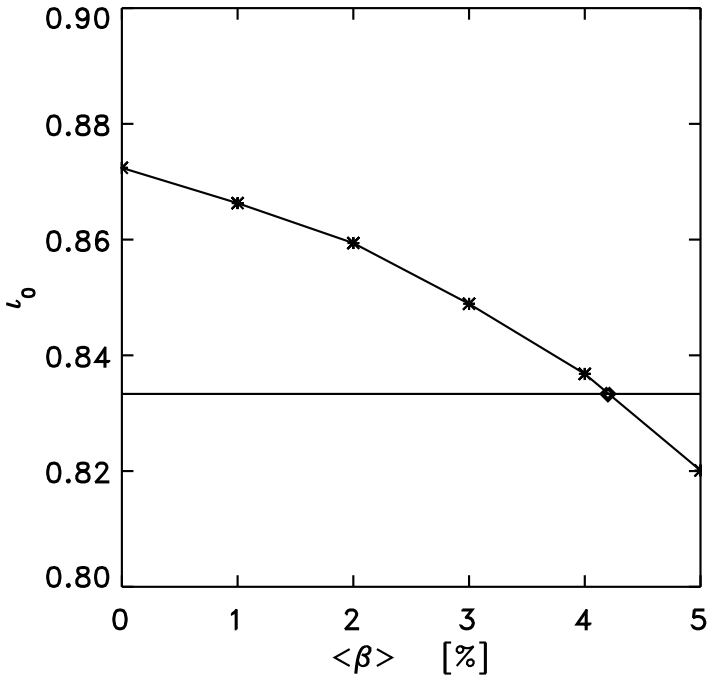

FIG. 15: Rotational transform on the magnetic axis versus the volume-averaged β-value. The stars mark the β-values for which equilibria have been computed. The horizontal curve indicates $\iota = 5/6$, while the diamond marks the β-value for which the rotational transform on the magnetic axis reaches $\iota = 5/6$.

- Mercier and resistive interchange criteria and local ballooning modes show stability up to $\langle\beta\rangle = 4\%$.
- For $\langle\beta\rangle = 4\%$ global ideal MHD stability studies show stability with a good safety margin.
- For $\langle\beta\rangle = 5\%$ Mercier and resistive interchange criteria show instability around the 5/6 resonance, and the local ballooning modes are even unstable at all plasma radii, e.g. at $\iota = 5/6$, 6/7, 7/8 and 8/9.

As has been shown in Fig. 15 the rotational transform in the plasma centre decreases with rising plasma pressure, so that the first low rational value arises in the plasma

centre for $\langle\beta\rangle \geq 4.2\%$. Using the NEMEC code for computing the plasma equilibrium no information about island sizes can be obtained, because the code assumes nested flux surfaces. Therefore, the equilibrium solution for $\langle\beta\rangle = 5\%$ containing the 5/6 resonance has to be considered as an approximation. In order to compute equilibria with islands other codes are needed, e.g. the PIES code [15 – 17]. Furthermore, up to now it could not be shown that local ballooning modes give a strong stability limit for low-positive-shear stellarators [18]. Because of these uncertainties the choice of $\langle\beta\rangle = 4.2\%$ as MHD stability limit is quite conservative, but, nevertheless, fulfills the requirements of a HELIAS reactor.

Equilibrium and stability properties of the Helias reactor solely depend on the β profile while confinement and fusion power output depend on the details of the temperature and density profiles. Peaked β profiles are more favourable for optimizing the fusion power output. A parameter set which is compatible with a stability limit of $\langle\beta\rangle = 4.2\%$ is given in Table III.

TABLE III: Design values of the reactor plasma.

Magnetic field	4.75	T
Peak temperature $T(0)$	14	keV
Peak density $n(0)$	$2.4 \cdot 10^{20}$	m^{-3}
Average beta $\langle\beta\rangle$	4.2	%
Peak beta $\beta(0)$	10.3	%
Fusion power	2.9	GW
Confinement time	2.1	s

This example is not unique, however it demonstrates that this MHD stability limit is compatible with the requirements of an attractive Helias reactor. In summary, the present analysis of MHD equilibria and stability shows that the reduction of the Shafranov shift and the stability limits are sufficiently optimized for the purpose of a Helias reactor.

REFERENCES

[1] HIRSHMAN, S.P., MEIER, H.K., Phys. Fluids **28** (1985) 1387.

[2] HIRSHMAN, S.P., Lee, D.K., Comput. Phys. Commun. **39** (1986) 161.

[3] HIRSHMAN, S.P., van RIJ, W.I., MERKEL, P., Comput. Phys. Comm. **43** (1986) 143.

[4] MERKEL, P., J. Comput. Phys. **66** (1986) 83.

[5] STRUMBERGER, E., Nuclear Fusion **37** (1997) 19.

[6] NÜHRENBERG, J., ZILLE, R., in Proc. Workshop on Theory of Fusion Plasma, Varenna 1987, Eds. A. Bondesin, E. Sindoni, F. Troyon, 1988, EUR 11336 EN, 3.

[7] NÜHRENBERG, C., Phys. Fluids **B5** (1993) 3195.

[8] BOOZER, A., Phys. Fluids **23** (1980) 904.

[9] BEIDLER, C.D., et al., Proc. 16th In. Conf. on Fusion Energy, Montreal 1996, IAEA, Vienna 1997, **Vol. 3**, 407.

[10] HIRSHMAN, S.P., WHITSON, J.C., Phys. Fluids **26** (1983) 3553.

[11] MERCIER, C., in Plasma Physics and Contr. Nucl. Fusion Res. 1961, Nucl. Fusion 1962 Suppl. 2, IAEA, Vienna (1962) 801.

[12] GLASSER, A.H., GREENE, J.M., JOHNSON, J.L., Phys. Fluids **18** (1975) 875.

[13] NÜHRENBERG, J., ZILLE, R., Proc. 12th EPS Conf. on Contr. Fusion and Plasma Physics, Budapest 1985, EPS, Vol. **9F**, Part I, 445.

[14] NÜHRENBERG, C., Phys. Plasmas **3** (1996) 2401.

[15] REIMAN, A.H., GREENSIDE, H.S., Comput. Phys. Commun. **43** (1986) 157.

[16] REIMAN, A.H., GREENSIDE, H.S., J. Comput. Phys. **87** (1990) 349.

[17] ARNDT, S., MONTICELLO, D.A., REIMAN, A.H., Proc. 24th EPS Conf. on Contr. Fusion and Plasma Physics, Berchtesgaden 1997, EPS, Vol. **21A**, Part IV, 1661.

[18] SCHWAB, C., Proc. 20th EPS Conf. on Contr. Fusion and Plasma Physics, Lisboa 1993, EPS, Vol. **17C**, Part I, 417.